# Transient Flow Uniformity Evolution in Realistic Exhaust Gas Aftertreatment Systems using 3D-CFD

N.B. When citing this work, cite the original published paper.

(article starts on next page)

# Transient Flow Uniformity Evolution in Realistic Exhaust Gas Aftertreatment Systems Using 3D-CFD

Pratheeba Chanda Nagarajan[1] · Henrik Ström[2] · Jonas Sjöblom[1]

## Abstract

To precisely control a vehicle powertrain to minimize emissions, accurate and detailed models are needed to capture the spatio-temporal variability of the variables of interest. The aim of this work is to analyze flow and temperature fields in a geometrically realistic — and thus complex — exhaust gas aftertreatment system under transient conditions. The spatio-temporal response of these fields to upstream step changes is predicted using three-dimensional unsteady Reynolds-averaged Navier-Stokes (URANS) $\kappa - \omega$ simulations where the catalytic converter is described as a porous medium. A catalytic converter geometry with a 90°-bend and a partially dead volume is used to demonstrate the effects of time-resolved flow maldistribution on the profiles of velocity and temperature. Two sets of transient simulations in terms of step changes in velocity and temperature are performed. Uniformity indices are used to characterize the distribution and variability of the different catalyst channels under transient conditions. The evolution of the uniformity indices as functions of time and axial distance into the catalyst are calculated at different cross-sectional planes. The results show that the evolution of the temperature uniformity is rate controlling, continuously modulating the otherwise much faster flow uniformity response via the fluid properties. The temperature uniformity time scale is determined by the balance of flow, thermal inertia, and the heat losses from the system. The interplay between pressure drop and heat losses governs the transition to the new steady state in uniformity. These types of transient simulations and analyses can contribute essential information when developing reduced-order engineering models to represent the spatio-temporal variability in exhaust aftertreatment systems, in particular during rapid events such as cold start.

**Keywords** Flow maldistribution · Transient simulation · RANS · Thermal residence time · Heat loss · Representative channels

## 1 Introduction

Transport emissions account for a majority of pollutants in the air and they affect ecosystem and climate changes [1], besides affecting human health [2]. The emissions contain

✉ Henrik Ström
   henrik.strom@chalmers.se

✉ Jonas Sjöblom
   jonas.sjoblom@chalmers.se

   Pratheeba Chanda Nagarajan
   pratheeba.chandanagarajan@chalmers.se

[1] Division of Combustion and Propulsion Systems, Department of Mechanics and Maritime Sciences, Chalmers University of Technology, Gothenburg 41258, Sweden

[2] Division of Fluid Dynamics, Department of Mechanics and Maritime Sciences, Chalmers University of Technology, Gothenburg 41258, Sweden

carbon dioxide ($CO_2$), carbon monoxide (CO), unburned hydrocarbons (HC), particulate matter (PM), and oxides of nitrogen ($NO_x$). Emissions create both short-term and long-term health effects [2]. These emissions from the engine are treated by catalytic converters to reduce ambient air pollution [3]. To regulate the emissions that are emitted in the tail pipe, legislation was introduced in the early 1990s and is since then becoming increasingly stringent [4]. To achieve such significant reduction (even at the local emissions level), we need to understand the source of emission origin and its path through the catalytic converters until it is discharged at the tail pipe.

The exhaust from the engine is sent through catalytic converters to meet the requirements of the emission legislation. These catalysts are usually placed in series that are grouped as an exhaust aftertreatment system (EATS) [5]. Catalytic converters contain platinum group metals as active catalysts that convert CO to $CO_2$, reduce $NO_x$ to nitrogen, and oxidize unburned hydrocarbons to $CO_2$ [3]. In this way, engine-out

emissions flow through one or more aftertreatment devices before getting discharged as tail pipe emissions.

Catalytic converters are placed after the engine, and get heated up by the temperature of gases from the engine. During the startup of the engine, the catalyst is cold, and does not function (light off) instantly due to its thermal mass. The emissions during the warm-up phase of the catalyst account for a significant amount of the emissions. A measure of cold start emissions is obtained by measuring the mass of emissions emitted at the ambient temperature for a kilometer run by the vehicle.

To increase the efficiency of the catalyst, different configurations such as close-coupled catalysts and under-body catalytic converters are applied [6]. During cold start, close-coupled catalysts, due to the proximity to the engine, perform better than the under-body catalytic converters [7]. The placement of the catalytic converters in the powertrain is one of the reasons of flow maldistribution. One other reason is the pulsating behavior of the engine-out emissions that arise due to changes in engine operating conditions [8]. Vehicles also need to adhere to Real Driving Emissions (RDE) levels, which were first introduced in EU VI(c) norms. In a RDE test, the vehicle is driven in different real-time conditions that include driving on rural and urban roads, at high and low altitudes, at different ambient temperatures, highways, and varying payloads [9].

To achieve very low emissions in generic as well as difficult conditions during cold start and RDE conditions, improved understanding of the processes inside the catalytic devices is required. Motivation for near-zero emissions drives research advances in experimental design and investigations of EATS, improved models capturing better physics, and efficient materials for catalysts. Computational fluid dynamics (CFD) simulation becomes an indispensable tool for comprehensive understanding of the chemistry and physics. In particular, CFD may inform reduced-order modeling owing to its innate ability to handle varying degrees of complexity and accuracy, examining simple to complicated geometries.

A monolithic honeycomb catalytic converter essentially consists of multiple parallel channels through which gases flow. The walls of the converter are coated with active catalytic material. The residence time of the reactant gas affects the conversion. Between channels, only energy transfer in the form of heat occurs, without exchange of mass. Therefore, a very simple and efficient way of modeling the catalytic converter is to use a single channel that is representative of all channels of the monolith. Solutions to balance equations of continuity, momentum, energy and species transport, and reaction provide the complete profiles of velocity, temperature, and concentration of the EATS. This is well known as the single-channel model (SCM). There are many studies in literature on modeling aspects of SCM and here

we mention only a few. Young and Finlayson have solved for the axial and radial variations of temperature in a monolith, treating it as Graetz problem using orthogonal collocation [10, 11]. Oh and Cavendish sought solution to transient convection-diffusion-reaction problems in a monolith [12, 13].

Since its inception, many improvements have continuously been added to the classical SCM. These include a variety of additional physical processes. For example, Santos and Costa developed an SCM using an effectiveness factor, where they include species diffusion inside the washcoat [14]. Siemund et al. proposed a 1D model with oxygen storage, accounted for transverse diffusion in the converter by a film model, and showed the range of the frequency sampling rate for the experimental data of CO conversion to be compared with the simulation results [15]. Hoebink et al. used a first-principles model with detailed kinetics to predict the light-off curves as a function of feed temperature [16]. Holder et al. [17] studied the performance of a 1D heterogeneous model with global kinetics. They validated the results for a fresh catalyst and extended the same to an aged catalyst without any further tuning. Lundberg et al. [18] developed a 1D+1D discretization to better capture mass-transfer effects and Walander et al. [19] proposed a model that also discretizes the washcoat corners. Koltsakis and Stamelos used a 2D model and global kinetics to simulate for different flow patterns at the inlet of the monolith [5]. Other works use correlations for the Nusselt and Sherwood numbers to relate to the transport processes between the bulk and the wall [15, 20]. The aforementioned works discuss various improvements in SCM modeling without a detailed discussion about the flow distribution in the catalytic converters. However, a uniform flow distribution is a prerequisite for the traditional SCM approach.

If a reduced-order model should be successful in representing the complete catalytic reactor, the degree of flow uniformity needs to be known. Consequently, several steady-state flow uniformity studies have been performed over the years [21–25]. Weltens et al. [21] performed simulations to show that the angle of diffuser of the inlet of the monolith influences flow uniformity and validated the same with 3D CFD simulations. Holmgren et al. [22] showed that flow uniformity could be modified by shaping the inlet part of catalytic converter. Agrawal et al. [23] and Dammalapati et al. [24] performed steady-state simulations involving reactions represented by global kinetics. They found that flow maldistribution affects conversion under non-isothermal conditions. Chakravarthy et al. [26] performed transient simulations to study the effect of flow maldistribution under cold-start conditions.

The SCM models previously described [10–20] are elegant in the sense that they capture the trends in the axial direction, and popular owing to their lower complexities and

computational costs, but, on the other hand, they provide no information about the channel-to-channel variations arising due to the non-uniform nature of flow and temperature. They can be used as predictive tools within certain bounds or for studying qualitative trends.

Several software are available for evaluating the flow field or predicting the conversion in the catalytic converters. To name a few, 1D models are solved with LOGESOFT, CHEMKIN, and AVL-BOOST. 2D or quasi 2D models use GT-Power. 3D simulations use ANSYS FLUENT, STAR-CCM+, and AVL-FIRE for evaluating the flow field. Reaction kinetic mechanisms are the source terms for evaluating the species concentrations.

The previous works on flow uniformity [22–24] in the literature have not — to the best of our knowledge — neither attempted to elucidate the full transient spatio-temporal effects on flow uniformity arising due to time-varying exhaust conditions, nor quantitatively investigated the interpretation of the uniformity index as a reduced-order descriptor of the two-dimensional degree of uniformity in a three-dimensional geometry. Due to increasingly more stringent emission norms, future SCM-type models would benefit from being informed of three-dimensional distribution information under generic and difficult conditions like RDE and cold starts.

## 2 Theory of Maldistribution

SCM forms the basis of many applications in emissions control. The representative channel should, in theory, be identical to all other channels and at all times. Alternatively, the representative channel could represent the mixed-cup average channel. However, given the strong non-linearity and coupling inherent to the problem, the latter approach is practically impossible for realistic kinetics.

Gases, while flowing through the channels, transport heat by advection. The channels do not allow exchange of mass between them but do transfer energy by conduction in the solid and to the ambient through diffusive heat transport from the wall. In an ideal condition, the flow will be uniform in all the channels. If all channels receive identical velocity and temperature, and have same catalyst loading, the profiles of velocity, temperature, and concentration will be identical (in the absence of heat losses and heat interaction with neighboring/adjacent channels). Performance of the catalytic converter and adherence to emission legislation are evaluated from the conversion predicted by the SCM for this representative channel. If the incoming flow to the channels is not uniform, then the catalytic converter experiences flow maldistribution. Flow maldistribution affects catalyst performance (i.e., conversion) as well as ageing of the catalyst [27]. It therefore becomes imperative

to quantify flow maldistribution under transient conditions and when the EATS undergoes change from one steady state to another.

To quantify the uniformity of flow, an index called flow uniformity index (UI) is defined. Flow uniformity index is a non-dimensional scalar that expresses the variation of a given flow parameter, such as the velocity or the temperature over a surface, as a measure of the deviation from the mean value of the flow variable in question. It is expressed as the area-weighted average of the ratio of the deviation of the flow variable in a channel from the mean flow variable to the flow variable over all channels [22]. In this work, we choose to use the definition of uniformity index as defined by [28]:

$$\gamma_a = 1 - \frac{1}{2}\left(\frac{\sum\limits_{i=1}^{n} |\phi_i - \overline{\phi_a}| A_i}{\overline{\phi_a}\sum\limits_{i=1}^{n} A_i}\right) \tag{1}$$

where

$$\overline{\phi_a} = \frac{\sum\limits_{i=1}^{n} \phi_i A_i}{\sum\limits_{i=1}^{n} A_i} \tag{2}$$

where $\phi_i$ is the flow variable (velocity, temperature) in the face $i$, $\overline{\phi_a}$ is the area-weighted average of the flow variable, and $A_i$ is the area of face $i$.

For example, for a flow uniformity value of 0.95, the value of the relative deviation from the mean value (term within the brackets) will be 10%. Values much smaller than 1 indicate significant flow maldistribution. The shape of the inlet section of the EATS, the inertia of the flow, and certain other flow conditions (such as pulsations) affect the UI.

It should be noted that other definitions of uniformity indices are used in parallel by researchers [21, 23, 29]. The UI can be evaluated experimentally [21, 25] or estimated by simulation [21–23]. In a CFD framework, to evaluate the flow uniformity index (UI) and temperature uniformity index, the solution to the momentum equations and the energy equation are needed respectively.

This work addresses a CFD-based methodology to perform transient simulations to follow the flow distribution evolution over time by numerical simulations. Transient inlet velocity and temperature boundary conditions are used to represent the transitioning between states. The goals of the paper are to establish a methodology to perform and analyze transient flow simulation to (1) understand how the uniformity indices evolve during a transient event and to (2) elucidate the coupling between the velocity UI and the temperature UI. Most importantly, we perform this analysis for a complex geometrical setting relevant to realistic aftertreatment system

configurations, where the monolith section receives its inflow after a bend and a partially dead volume.

This work addresses the simulations to obtain velocity and temperature fields under non-reactive non-isothermal transient conditions. The organization of the work is as follows: we first present the experimental details. Thereafter, the model for the CFD simulations, along with the boundary conditions, is presented. The solution methodology forms the next section. The analyses that we then perform are of the flow distribution with the help of visualizations such as histograms and contour plots. We provide the discussions and implications of the findings. Finally, a summary of the conclusions is presented.

## 3 Experimental Section

For the inferences of the current work to be directly relevant to realistic aftertreatment systems, the geometry must not be trivial and there have to be realistic heat losses. We, therefore, use a dedicated experimental setup to acquire real-world data on the thermal behavior of the specific geometry adopted. The test catalytic section consists of diesel oxidation catalyst (DOC) housed to get an "academic exhaust aftertreatment system." The advantage of such a system is that it is very analogous to industrial EATS, exhibiting important features like heat losses and bends. These features need to be accounted for and in transient operation.

### 3.1 Test Section

The geometry used for this study has two sections of constant cross-section, an inlet section and a horizontal section. The inlet section is a vertical section, having the dimensions 60 cm length and 3 cm in diameter. This is connected to the horizontal section which is 25 cm long and 10 cm in diameter. The flow from the vertical section enters the horizontal section at an angle of 90°. The horizontal section also houses a catalytic section, with a DOC of 9.5 cm diameter and 9 cm length. The DOC has 400 cells per square inch (cpsi), and a precious metal loading of 10 g/ft$^3$. The washcoat loading is 2.6 g/inch$^3$. The catalyst is covered by an insulation layer of glass wool. The entire structure is contained in a stainless steel casing. We refer to this geometry as the academic EATS. The flow from the vertical inlet section induces a flow distribution at the entry section of the academic EATS. The geometry is shown in Fig. 1 and the details are presented in Table 1.

### 3.2 Instrumentation Details

A set of mass-flow controllers allows to set the desired flowrate. The rated flowrates are 1000 lpm, 200 lpm, and 20 lpm at standard conditions. The setup is also fitted with a
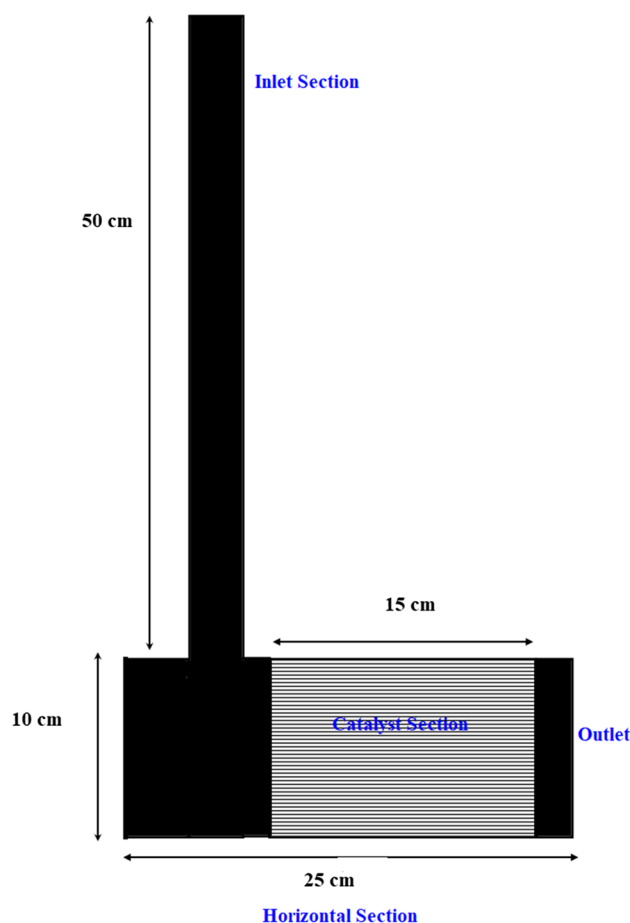


**Fig. 1** Overview of the academic EATS. The dark sections represent the non-catalytic regions and the shaded region is the catalyst. The domain is half-symmetric (the illustrated cross-section represents a symmetry plane)

**Table 1** Geometry details

| Parameter | Variable | Value |
|---|---|---|
| Diameter of inlet section | $D_{inlet}$ | 3 cm |
| Length of the inlet section | $l_{inlet}$ | 60 cm |
| Diameter of horizontal section | $D_{hor}$ | 10 cm |
| Length of horizontal section | $l_{hor}$ | 25 cm |
| Diameter of DOC with insulation | $D_{cat}$ | 10 cm |
| Length of DOC (cm) | $l_{cat}$ | 15 cm |

temperature-controlled heater for heating of the gases. The temperature to which the gases can be heated is limited by the rated power of the heater (3 kW). The catalyst is also insulated with layers of insulating glass wool. The catalytic section is fitted with K-type thermocouples on the inlet side (4 sensors) and the exit side (8 sensors). Care is taken so that the thermocouples are placed evenly and symmetrically (cf. [30]). An in-house LabVIEW system provides the

control and data acquisition. The placement of thermocouples and the schematic of the experimental rig is shown in Fig. 15. Table 5 shows the placement coordinates for all the thermocouples.

# 4 Modeling of the Academic EATS

This section presents the details of the computational mesh, the modeling methodology, and the equations that are solved. Step changes in velocity and temperature are the forcing inlet functions for the transients through the system.

## 4.1 Geometry and Mesh

The geometry that is used for the simulation is the one presented in Section 3.1 and Fig. 1. The computational mesh contains 700,388 structured hexahedral cells and takes advantage of the symmetry of the test section to only represent half of the physical domain of study.

## 4.2 Modeling Methodology

The geometry has two flow sections: non-catalytic pipe sections and a catalytic section that houses the monolith. The inlet conditions involve changes in velocity and temperature as function of time. The flow is non-adiabatic and non-reactive. The flow is from top to bottom and then from left to right. The pressure does not change much over the geometry and the flow is regarded as incompressible. We seek the profiles for velocity, temperature, and pressure for flow through these aforementioned sections. The solution is obtained by solving the coupled equations of continuity, momentum and energy under transient conditions.

Two sets of simulations are performed, steady-state and transient simulations. The simulations are performed with the CFD-software ANSYS FLUENT 2021R2. Steady-state simulations are performed to tune the heat loss to the ambient through heat transfer coefficients applied in the wall heat flux boundary conditions. Experimental values of temperatures were logged using thermocouples, by passing heated air at the tested flowrates. The temperatures measured were compared with that predicted by the simulations. This provided a means to tune heat transfer coefficients for further use in the transient simulations. The details of these results are shown in Appendix B. A step change in velocity and temperature is provided as the transient inlet condition through user-defined functions (UDFs). The heat loss is accounted through the shell-conduction model. Radiation effects are insignificant at the operating conditions, and gravitational effects are neglected throughout.

## 4.3 Model Equations for the Non-catalytic Section

The flow is turbulent in the sections other than the catalyst section. The flow undergoes transition and becomes laminar in the catalyst section. Unsteady Reynolds-averaged Navier-Stokes (URANS) equations are solved along with turbulence scalar equations. A suitable turbulence model such as the SST $\kappa - \omega$ model is chosen as this can be used for low-Reynolds-number flows and perform relatively well for flows influenced by adverse pressure gradients [31]. Literature shows k-$\epsilon$ model is also used, but is known to overpredict the near-wall effects [31]. A pressure-based solver is used for the solution. The following are the equations for the mean flow in the EATS:

Equation of Continuity:

$$\frac{\partial \rho}{\partial t} + \nabla \cdot \left( \rho \overline{U} \right) = 0 \tag{3}$$

Equation of Motion:

$$\rho \left[ \frac{\partial \overline{U}}{\partial t} + \left( \overline{U} \cdot \nabla \right) \overline{U} \right] = -\nabla \overline{p} + (\mu + \mu_t) \nabla^2 \overline{U} - \nabla \cdot \left( \frac{2}{3} \rho \kappa I \right) \tag{4}$$

Equation of Energy:

$$\frac{(\partial \rho C_p \overline{T})}{\partial t} + \nabla \cdot (\rho C_p \overline{T} \, \overline{U}) = \frac{\partial \overline{p}}{\partial t} + \overline{U} \cdot \nabla \overline{p} - \nabla \cdot q_i + \overline{\Phi} \tag{5}$$

where $q_i$ is the heat flux vector and $\Phi$ is the dissipation function.

Closure $\kappa - \omega$ equations:

$$\frac{\partial(\rho\kappa)}{\partial t} + \nabla \cdot \left( \rho\kappa\overline{U} \right) = \nabla \cdot \left( \left( \mu + \frac{\mu_t}{\sigma_k} \right) \nabla\kappa \right) + \left( 2\mu_t S \cdot S - \frac{2}{3} \rho\nabla\kappa\overline{U}I \right) - \beta^* \rho\kappa\omega \tag{6}$$

$$\frac{\partial(\rho\omega)}{\partial t} + \nabla \cdot \left( \rho\omega\overline{U} \right) = \nabla \cdot \left( \left( \mu + \frac{\mu_t}{\sigma_\omega} \right) \nabla\omega \right) + \gamma_1 \left( 2\rho S \cdot S - \frac{2}{3} \rho\omega\overline{U}I \right) - \beta_1 \rho\omega^2 \tag{7}$$

Here, the strain tensor $S$ in Eqs. 6 and 7 is $S = \frac{1}{2} \left( \nabla\overline{U} + (\nabla\overline{U})^T \right)$. Further information and explanation about the $\kappa - \omega$ model can be found in [32].

## 4.4 Model Equations for the Catalytic Section

The catalyst is modeled as a porous medium inside which laminar flow is enforced. The porous approximation significantly lowers the computational load compared to resolving the flow in every channel of the monolith. In the porous approximation employed here, the additional pressure drop arising due to the flow through the catalyst section is described as a viscous resistance. Source terms that account for this pressure drop are added to the momentum balance equations [28]:

$$S_i = -C_i \mu \overline{U}_i \qquad (8)$$

The energy equation for the porous media is given by [28]:

$$\frac{\partial}{\partial t}\left(\epsilon \rho_f E_f + (1-\epsilon)\rho_s E_s\right) + \nabla \cdot \left(\vec{v}\left(\rho_f E_f + p\right)\right)$$

$$= \nabla \cdot \left[k_{\text{eff}}\nabla T - \left(\sum_i h_i J_i\right) + (\overline{\overline{\tau}} \cdot \vec{u})\right] + S_f^h \qquad (9)$$

The coefficient of the viscous resistances $C_i$ is inversely proportional to the square of the hydraulic channel diameter. The pressure drop observed from the output can be matched and tuned to get accurate values, or, alternatively, pressure-drop measurements as a function of flowrate can yield these constants. Here, the value of the viscous resistance used in the simulations is $2.74 \cdot 10^7\,\text{m}^{-2}$ in the main flow direction [33] and higher by three orders of magnitude in the other two directions. A check on the velocity fields for the X- and Y-velocities in the catalyst section was carried out to ensure there was negligible flow in the radial direction. The pressure drop over the monolith obtained in this way is 120 Pa (at 500 lpm) and 242 Pa (at 948 lpm).

### 4.5 Initial Conditions and Boundary Conditions

The inlet conditions include the transient velocity and temperature applied at the velocity-inlet boundary condition. These conditions are provided through a UDF that describes them as a function of time.

The turbulence boundary conditions are obtained from a turbulent intensity and a turbulent length scale. The turbulence intensity was assumed to be identical to $I_{turb} = 0.16 Re^{-1/8}$ and the turbulent length scale was set to 7% of the hydraulic diameter of the inlet duct.

The outlet boundary condition is specified as a pressure-outlet with zero gauge pressure, implying that pressure is fixed and all other variables have zero gradient normal to the outlet.

The no-slip boundary condition is enforced at the walls. The shell conduction model is used represent the layers of insulation and heat loss to the ambient. The thermal properties of the monolith, insulation, and metal casing are input to the shell conduction model. A tuned value of heat transfer coefficient was used to represent the convective heat interaction.

### 4.6 Material Properties

Air is the working fluid and is assumed as ideal gas with temperature-dependent properties. Physical properties of air as a function of temperature were taken from NASA polynomials. The catalytic converter is made of cordierite. The physical properties for the catalyst are assumed anisotropic to reflect the presence of an extruded monolithic reactor. The porosity of the catalyst is 0.72, which is equal to its open frontal area (hence not to be confused with the wall porosity). The solid phase material properties are provided in Table 2.

### 4.7 Operating Conditions and Simulation Cases

The operating conditions prevailing at the two steady-states (SS1 and SS2) are provided in Table 3. The transient simulations represent either the start from zero velocity and ambient temperature to SS1 or the transition from SS2 to SS1, as detailed in Table 4.

### 4.8 Solution Methodology

The geometry is half-symmetric about the middle plane. The semi-implicit pressure-linked equation (SIMPLE) method is used to solve for pressure and velocity. The convective terms were discretized using the first-order upwind scheme for momentum, $\kappa$, $\omega$, and energy. Pressure discretization was second-order accurate. Diffusional terms were discretized with a second-order accurate central differencing scheme. A first-order implicit formulation was used for the transient terms. The default coefficients of the SST $\kappa - \omega$ model were also used with corrections for low-Reynolds number and shear flow. Mesh regions that showed significant gradients were refined as needed, and the refined grid was used thereafter for obtaining the solutions. Iterative convergence was assessed through scaled residuals that had to be reduced by at least three orders of magnitude within the iterations of a time step. Total mass and energy balances were additionally checked for the steady states.

## 5 Results and Discussion

The two transient simulation cases under analysis here are labelled `0 to SS1` and `SS2 to SS1`, respectively. These are step changes in velocity and temperature at the inlet of the geometry. Plane locations within the catalyst are used to illustrate and explain the evolution of the uniformity indices and link these to the transient flow and thermal behaviors. The chosen planes are pictured in Fig. 2.

**Table 2** Material properties

| Material | Density | Specific heat capacity | Thermal conductivity |
|---|---|---|---|
| | $\rho$ (kg/m$^3$) | $C_p$ (J/kg,K) | $k$ (W/m,K) |
| Stainless steel | 8000 | 502.48 | 16.27 |
| Cordierite | 279 | 1050 | 1.8, 0.9, and 0.9[1] |
| Insulating mat | 200 | 1080 | 0.057 |
| Glass wool | 100 | 840 | 0.03 |

[1]Anisotropic thermal conductivities in three coordinate directions

**Table 3** Operating conditions

| Flow parameter | Steady state 1 | Steady state 2 |
|---|---|---|
| Volumetric flowrate at STP (lpm) | 500 | 948 |
| Operating temperature (°C) | 100 | 93 |
| Velocity at operating conditions (m/s) | 11.8325 | 22.0135 |
| GHSV of the catalyst ($h^{-1}$) | 39,189 | 74,302 |
| Residence time (s) | 0.181 | 0.097 |

## 5.1 Histograms

Firstly, we start with the analysis of the histograms of velocity and temperature in the catalyst at the steady state denoted SS1. To understand the complex nature of flow and thermal uniformity, contours of two flow variables, viz., velocity and temperature, are chosen along with the histograms of the quantities.

The velocity variation in the catalyst is shown in Fig. 3. The velocity histogram shows a bimodal distribution and it is skewed to towards higher velocities. The bimodal nature is also reflected in the contour. The contour shows two distinct color regions (red and green zones) for high velocity and low velocity. The flow commences from the inlet in the vertical section and travels through a 90°-bend, enters the catalyst zone, and finally exits through the outlet. The flow from the vertical duct emerges as a jet before it deflects in the horizontal section. The fluid experiences pressure drop due to friction and minor losses and flow through a convergent section in the catalyst. The temperature field also influences the physical properties of the flowing fluid. The low-velocity section is a result of the frictional pressure drop and the adherence to continuity as the high-speed jet passes through the lower catalyst section.

The temperature variation is shown in Fig. 4. The temperature histogram shows a more distinct bimodal pattern, with two peaks and a spread of values between the peaks. The contour of temperature shows two distinct temperature regions in the center and a more diffuse color towards the periphery. The boundary of the geometry is exposed to ambient conditions and thus to heat losses. The flow from the inlet section ensues as a jet. The lower section has a

**Table 4** Simulation cases

| Case name | 0 to SS1 | SS2 to SS1 |
|---|---|---|
| Starting time (s) | 0 | 0 |
| Initial velocity (m/s) | 0 | 11.8325 |
| Initial temperature (°C) | 20 | 100 |
| Step change time (s) | 0 | 20 |
| Velocity at step change (m/s) | 22.0135 | 22.0135 |
| Temperature at step change (°C) | 93 | 93 |
| Simulation stop time (s) | 35 | 35 |
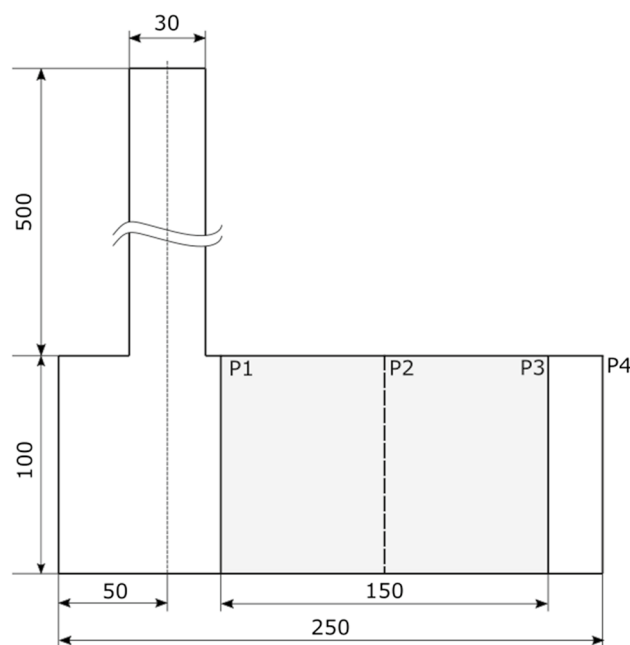
**Fig. 2** Plane locations for the analysis of results. Plane P1 is at the entry of the catalyst, P2 at the center, and P3 is the exit of the catalyst and P4 is the domain outlet

higher flowrate and hence is not cooled as effectively as the flow in the upper section of the catalyst. The bimodal peaks are a result of the interplay between the convective energy transport in the axial direction and the conductive transport in the radial direction. The solid sections of the catalyst are more effective in conducting the heat as compared to the gas. The contour shows a high-temperature region, which is a result of the hot jet.

Catalytic converters are housed compactly in the exhaust line of an automobile. The placement usually induces bends and provoke broad residence time distributions. From the histograms of velocity and temperature, it is hard to specify a single value of velocity or temperature as the representative value that could be used for an SCM. The spread is significant in terms of velocity and temperature. This emphasizes that flow distribution information is required in modeling for better prediction of velocity and temperature and possibly concentration.

More specifically, it can be noted from Figs. 3 and 4 that the locations contained within the region encapsulating $\pm 1\%$ the average velocity or temperature are situated in different parts of the monolith cross-section. Whereas the region of (close to) average temperature can be found above the hot jet and away from the walls, the region of (close to) average velocity is limited to two narrow bands above the bottom jet and below the upper low-speed region. Therefore, the channels receiving the average velocity are not the channels receiving the average temperature. As a consequence,

**Fig. 3** Distribution of velocity plotted at the steady state SS1. The left side of the figure is a histogram of velocities extracted over the catalyst and the right side represents a contour showing the velocity magnitude in a plane (P2) at the center of the catalyst normal to the main flow direction
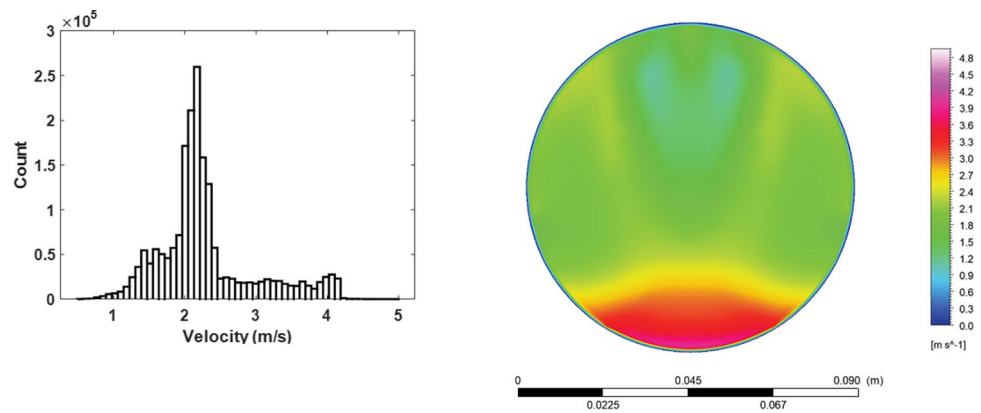
**Fig. 4** Distribution of temperature plotted at the steady state SS1. The left side of the figure is a histogram of temperatures extracted over the catalyst and the right side represents a contour showing temperature in a plane (P2) at the center of the catalyst normal to the main flow direction
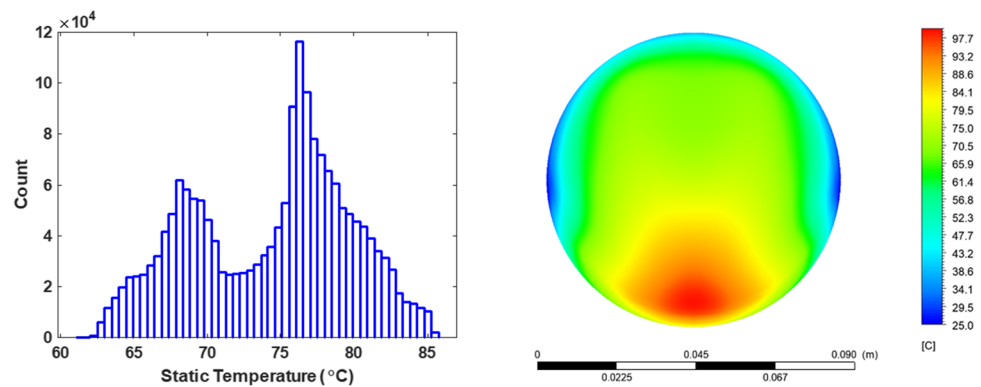
the mixed-cup average conversion after the monolith is not produced by the combination of the average velocity and the average temperature — it will in fact not necessarily be produced in any real-world channel at all.

## 5.2 Flow Uniformity Index

Uniformity indices (UIs) are plotted as a function of time for velocity and temperature in Fig. 5. The operating conditions for the two simulation cases are the ones listed in Table 3. To elucidate the scales of response times of the velocity UI and temperature UI and to show the evolution of the UI from one statistically steady state to another, the abscissa is chosen such that it represents a steady-state value. In the lower panel, the time from −2 to 0 s represents the process in the steady state 0 or SS2. Uniformity indices for the flow parameters are calculated on an area-weighted basis. The three planes shown in Fig. 2 are chosen for the visualization of the uniformity index evolutions.

The histograms in Figs. 3 and 4 showed the existence of a distribution in velocity and temperature in the catalyst at the final steady state SS1. The flow experiences mixing in sections after the bend, before the catalyst, in the partially dead

zone and also after the catalyst. It can be observed that the uniformity index values are higher for lower velocities and lower temperatures. At the same time, the temperature UI at the catalyst inlet is slightly higher than that at the outlet, whereas the velocity UI varies the other way around. The heat losses exacerbate the non-uniformity for the temperature field along the main flow direction inside the catalyst, whereas the velocity maldistribution at the catalyst entrance is modulated towards a more uniform configuration indirectly via temperature-drive effects on the fluid properties.

The ultimate UI values that are attained are dependent on the final state of the EATS. For example, the UIs attain the same values when moving from 0 to SS1 or from SS2 to SS1. The final UI after the transient is thus equal to the steady-state UI — at some point history effects have decayed.

Another feature that is worth noting is the shape of the curve of the velocity UI, in that the two transient cases both exhibit similar curves. But, for the temperature UI, the shape is dependent on the temperature history of the monolith, and the initial state thus has a much more pronounced role. The slope of the temperature UI curve changes as the flow moves inward in the catalyst zone. In Fig. 5(a), the fluid continuously loses heat to the ambient.
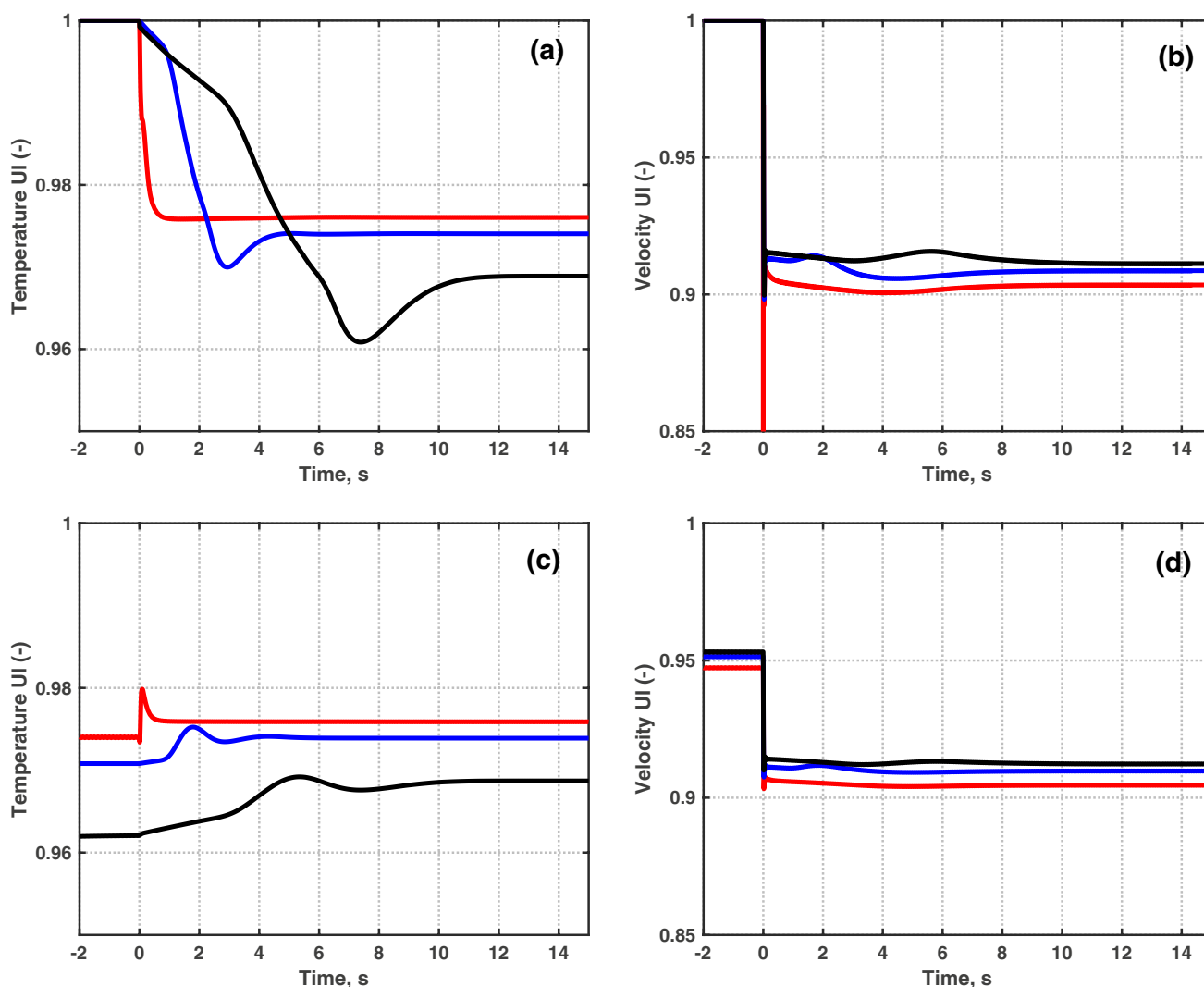
**Fig. 5** Temporal variation of uniformity indices. The top panels **a** and **b** represent the temperature and velocity UI plots for the simulation `0 to SS1` case and the lower panels **c** and **d** represent the same for the simulation `SS2 to SS1`. The location of the red line is the plane P1, blue and black follow the planes P2 and P3 respectively

The UI at plane P3 represents a larger thermal response that is a combination of conduction and convection. Referring to Fig. 5(c), the inlet fluid temperature has dropped at $t = 0$ s along with an increase in velocity. The temperature UI readings initially improve and then stabilize after an intermittent peak.

The UI plots also provide quantitative information on the flow response time and the thermal response time. The velocity field stabilizes rapidly, as can be seen from the vivid UI response around the step change. The thermal response time is much longer than that of the flow due to higher thermal mass of the system. Heat losses also add to the larger thermal time constant.

In Fig. 5(a, b), the plane P1 closest to the catalyst inlet has the highest temperature UI. As the fluid flows through

catalyst, it exchanges heat to the ambient and loses energy and hence attains lower and less uniform temperature.

It is interesting to note that the lowest attainable velocity is 0 m/s (no-flow condition), whereas the lowest attainable temperature in the simulation is the ambient temperature (20°C). The highest values are the inlet velocity and the inlet temperature. The temperature UI is formulated with a base reference temperature equal to the ambient temperature. Nevertheless, a value of 0.95 as the uniformity index for velocity and temperature does not translate to the same level of uniformity for the two variables. This is due to the fact that the uniformity index quantifies the variation in relation to the mean, and hence the UIs are not independent of base reference values. UI values based on different reference baseline values are discussed in Appendix C.

## 5.3 Pathlines

Figure 6 shows the pathlines of the flow. The following sections of the geometry are particularly noteworthy. The inlet section meets the horizontal section through a 90° -bend. The horizontal section extends asymmetrically on either sides on the axial direction, the dead-end section having a smaller volume than the catalytic section leading to the domain outlet. The flow impinges the horizontal section, before making the 90°-bend. Eventually the flow exits out after passing through the catalyst. The dead-end side causes recirculation streams that eventually joins the flow through the catalyst towards the exit. These recirculation remnants affect the movement of the gas and also affect the temperature profiles. The recirculation jets have longer residence times and therefore lose more heat.

## 5.4 Flow Fields of Velocity and Temperature

This section presents in-depth illustrations of the contours of velocity and temperature in the catalyst and at the outlet of the academic EATS for the case SS2 to SS1. The movement of the gas is the feature in the velocity contours, whereas the temperature contours show the cooling of the hot gas from the inlet, until the outlet of the academic EATS.

The contours are shown here for specific times. Such times of specific interest are identified from the UI plots, where there is a significant change in slope in either UI-signal.

Contours of velocity at planes P1, P2, and P3 are depicted in Figs. 7, 8, and 9. The fluid from the inlet passes through the vertical section, which also promotes some heat loss. The 90°-bend induces minor losses and causes flow separation. The fluid impinges as a jet that passes through the catalyst, with recirculation zones in the partially dead volume. We can see that the velocity in the monolith section is low compared to the velocity at the inlet, due to the expansion of the available cross-sectional area for the flow. The velocity field stabilizes very rapidly to changes in the inlet.

Contours of temperature at planes P1, P2, and P4 are shown in Figs. 10, 11, and 12, respectively. The hot air from the inlet travels through the vertical section. The upper lobe of the horizontal section, especially the monolith section, is relatively colder. The lower section experiences a larger flow than the upper section, and hence the cooling of the gas here is rather ineffective. The temperature flow field attains uniformity slower
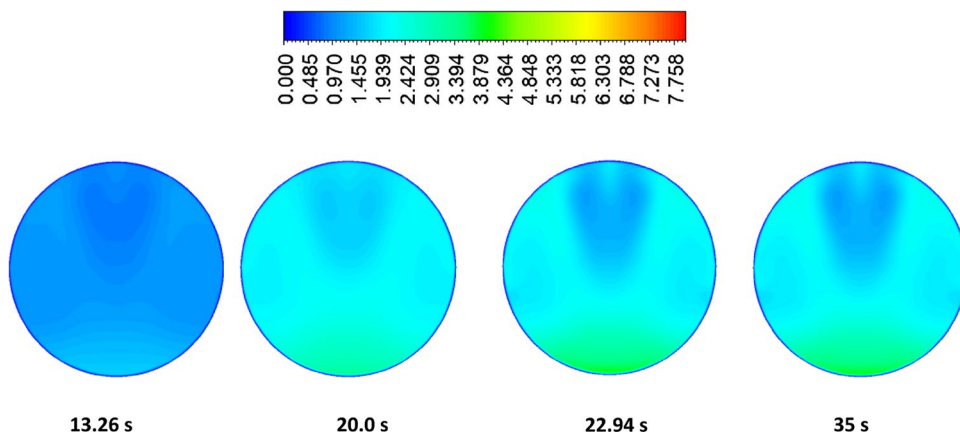


**Fig. 6** Pathlines of the flow inside the academic EATS
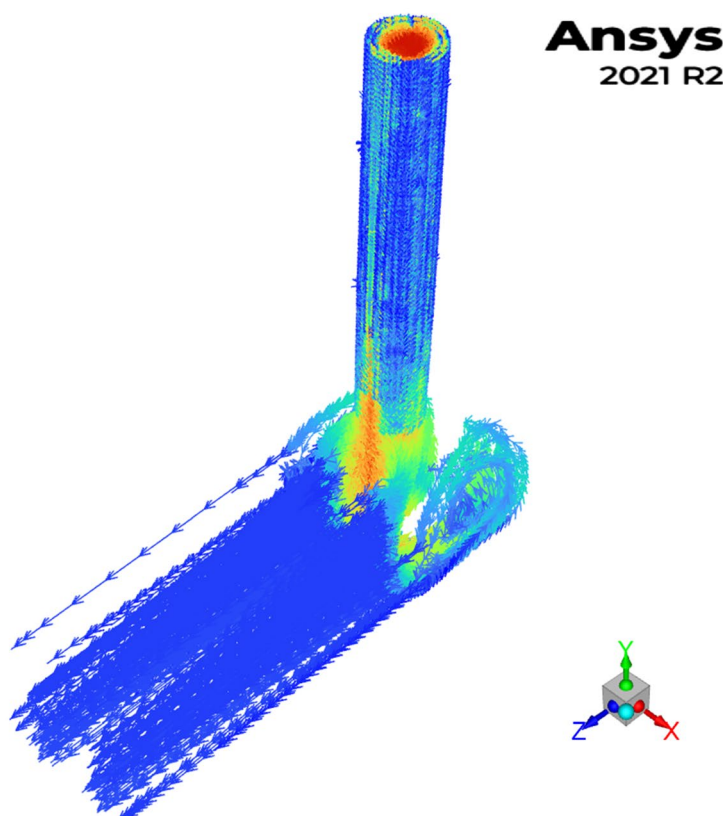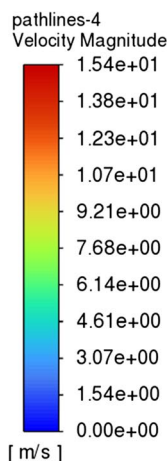
**Fig. 7** Contours of velocity at plane P1 (catalyst inlet) for the case SS2 to SS1. The time instances of the contours are shown below each contour. The colorbar shows the velocity values in meters per second
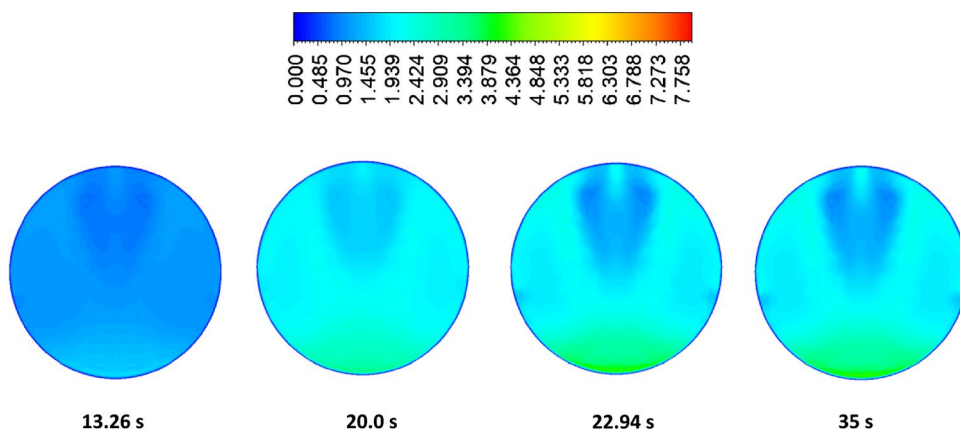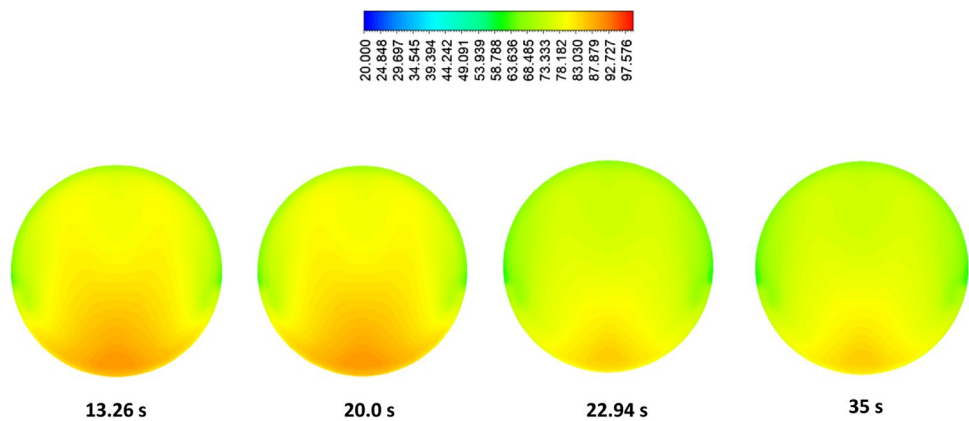


**Fig. 8** Contours of velocity at plane P2 (middle of catalyst) for the case SS2 to SS1. The time instances of the contours are shown below each contour. The colorbar shows the velocity values in meters per second



**Fig. 9** Contours of velocity at plane P3 (catalyst outlet) for the case SS2 to SS1. The time instances of the contours are shown below each contour. The colorbar shows the velocity values in meters per second
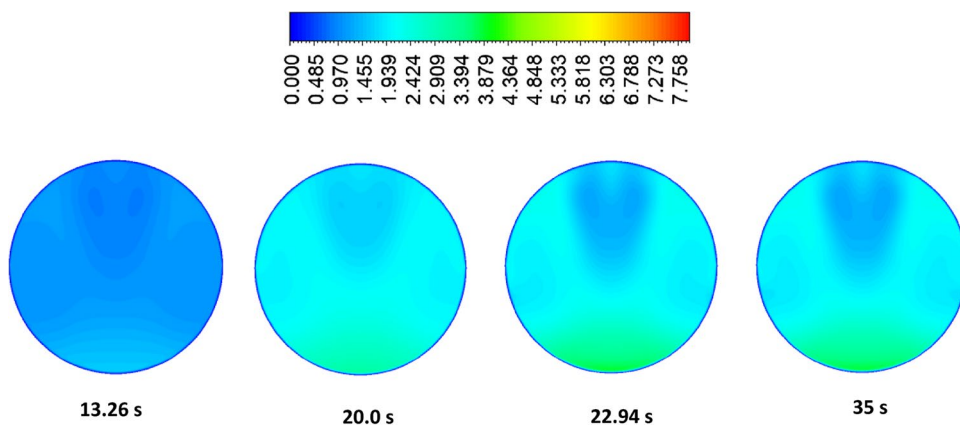


than velocity flow field due to larger thermal mass. The changes to the temperature field happen later towards the end of the catalyst as compared to the beginning of the catalyst, and the shift is much slower than what would be predicted from the flow response time of the system. At the same time, the incoming flow to the catalyst section governs the temperature uniformity inside it.

Additional contours of velocity and temperature are shown in Figs. 13 and 14. These are obtained at the plane in the horizontal section, after the bend and just before the inlet of the catalyst. The jet ensues from the inlet pipe and impinges on the bottom section with a high velocity, as shown by the green regions (the first two contours in the panel) and as yellow regions (the last two contours in

**Fig. 10** Contours of temperature at plane P1 (catalyst inlet) for the case SS2 to SS1. The time instances of the contours are shown below each contour. The colorbar shows the temperature values in degrees Celsius



**Fig. 11** Contours of temperature at plane P2 (middle of catalyst) for the case SS2 to SS1. The time instances of the contours are shown below each contour. The colorbar shows the temperature values in degrees Celsius
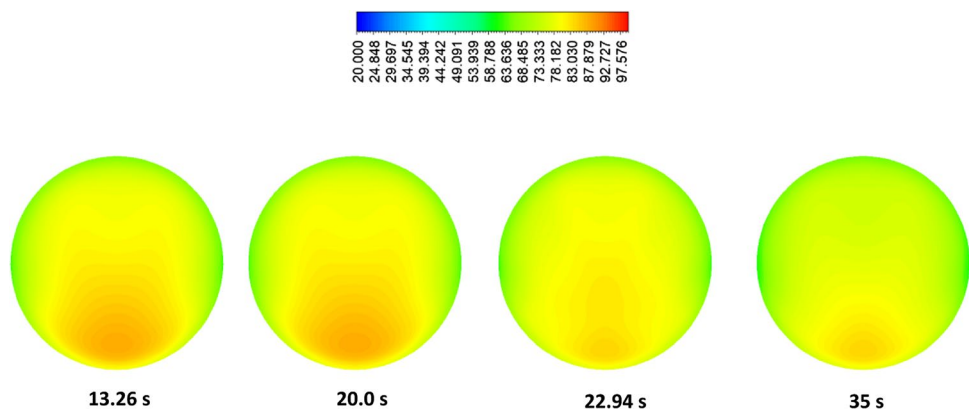


**Fig. 12** Contours of temperature at plane P4 (domain outlet) for the case SS2 to SS1. The time instances of the contours are shown below each contour. The colorbar shows the temperature values in degrees Celsius
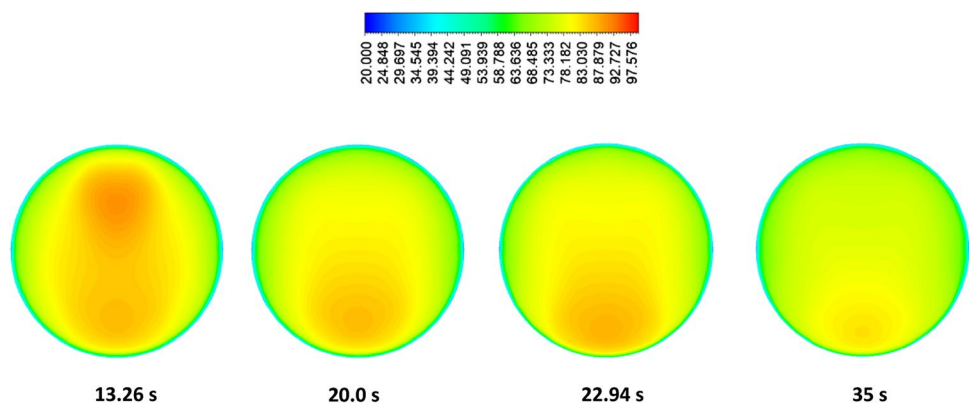


the panel) of the velocity contours. Similar temperature profiles are seen in the temperature contours too.

## 5.5 Implications for Reduced-order Modeling

Transient operations occur in the engine due to changes in operating conditions. The engine-out flow provides the inflow the catalytic converter. The analysis presented here, in the form of histograms and contours, shows that the flow behavior is complex and transient in nature. Even though the velocity distribution is quite narrow, the temperature distribution is very wide inside the monolith. This complex nature is a major bottleneck that restricts the applicability of the single-channel model (SCM) for realistic aftertreatment system configurations.

The uniformity index value is a scalar that contains information about the flow distribution. The velocity and temperature UI values attain equilibrium values when the temperature and velocity fields have attained steady states. During transient operation, they can be used to characterize the radial and axial non-uniformities.

**Fig. 13** Contours of velocity after the bend in the horizontal pipe, in a plane before the inlet plane P1 (inlet of catalyst) for the case SS2 to SS1. The time instances of the contours are shown below each contour. The colorbar shows the velocity values in meters per second



13.26 s          20.0 s          22.94 s          35 s
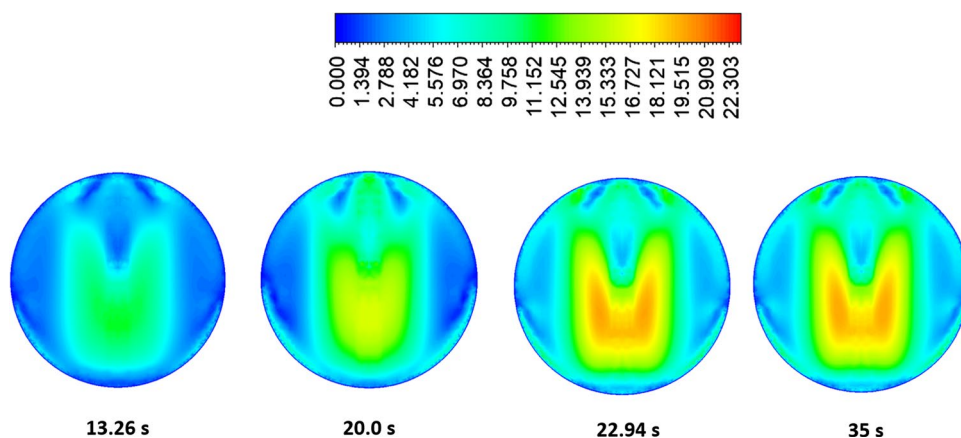
**Fig. 14** Contours of temperature after the bend in the horizontal pipe, in a plane before the inlet plane P1 (inlet of catalyst) for the case SS2 to SS1. The time instances of the contours are shown below each contour. The colorbar shows the temperature values in degrees Celsius



13.26 s          20.0 s          22.94 s          35 s
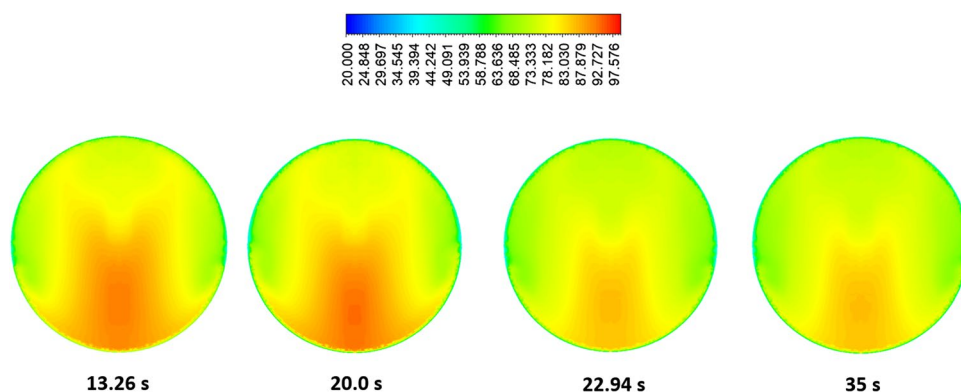
Three-dimensional CFD simulations could thus provide a route to mapping of UI behaviors for various well-defined transients. These UI behaviors could be used in informing SCM-variants of how to dynamically pick the representative inlet properties to reflect the mixed-cup performance of a catalyst in a realistic, complex geometry. There is a clearly identified need for models that are "in between" SCM and 3D-CFD in terms of complexity and computational cost. The transient analysis of UI-signals from 3D-CFD could provide the link needed in the future derivation of CFD-informed reduced-order 3D models.

# 6 Conclusion

Transient CFD simulations to characterize flow and temperature non-uniformities in realistic automotive aftertreatment systems have been carried out with step changes in both velocity and temperature. To demonstrate the role of bends and dead zones, a non-trivial geometry closely resembling a real EATS was chosen.

The catalyst was represented as a porous medium. RANS and porous medium models were used to simulate the non-reactive behavior of the catalyst under transient conditions. Dedicated experiments on temperature uniformity were performed, so that heat losses could accurately be accounted for in the simulations.

The results are analyzed with the help of histograms, contours of temperature and velocity in various planes in the catalyst region, and the temporal evolution of flow and temperature uniformity indices in various locations. The histogram of temperature shows pronounced bimodal behavior resulting from axial and radial gradients. The histograms and contours prove that the flow evolution under transient conditions is complex in that the mixed-cup average conversion will not necessarily be produced by any real-world monolith channel. It is thus in general not possible to represent all channels with a single velocity and temperature.

A methodology has been developed to understand the evolution of flow uniformity indices as a function of time. When the system moves from one steady state to another, the uniformity indices of the final steady state are ultimately reached. In the event that the inlet conditions are inherently unsteady (as could be expected in real driving scenarios), final steady states may not be reached and the transient response of the aftertreatment system will then always be influenced by its preceding temperature history. Uniformity index definitions are important to understand the role of these values in choosing representative channels. Heat losses and pressure drops are the two important

aspects that govern flow uniformity and influence its temporal evolution during transients. The thermal response time is slower, and the thermal behavior thus controls the time scale at which the system responds to changes in the driving. However, the evolution of the temperature field indirectly modulates the velocity field via the fluid properties, so that the velocity response continues to develop on time scales much longer than the flow response time.

The computational costs associated with reactive 3D-CFD simulations prohibit their use in virtual development on time scales at which real driving emissions are assessed. This analysis is thus intended as a precursor for developing reduced-order 1D+ models that can capture the 3D phenomena in catalytic converters at a lower computational cost, yet with improved accuracy to the conventional single-channel model (SCM). The current 3D-CFD setup can then be used to generate the flow uniformity data needed to train a reduced-order model in choosing an efficient number of representative channels to attain a pre-determined accuracy.

## Appendix A. Position of Thermocouples

The positions of the thermocouples are given in Fig. 15 and show the schematic of the experimental rig and the positions of the thermocouples as indicated in Table 5.
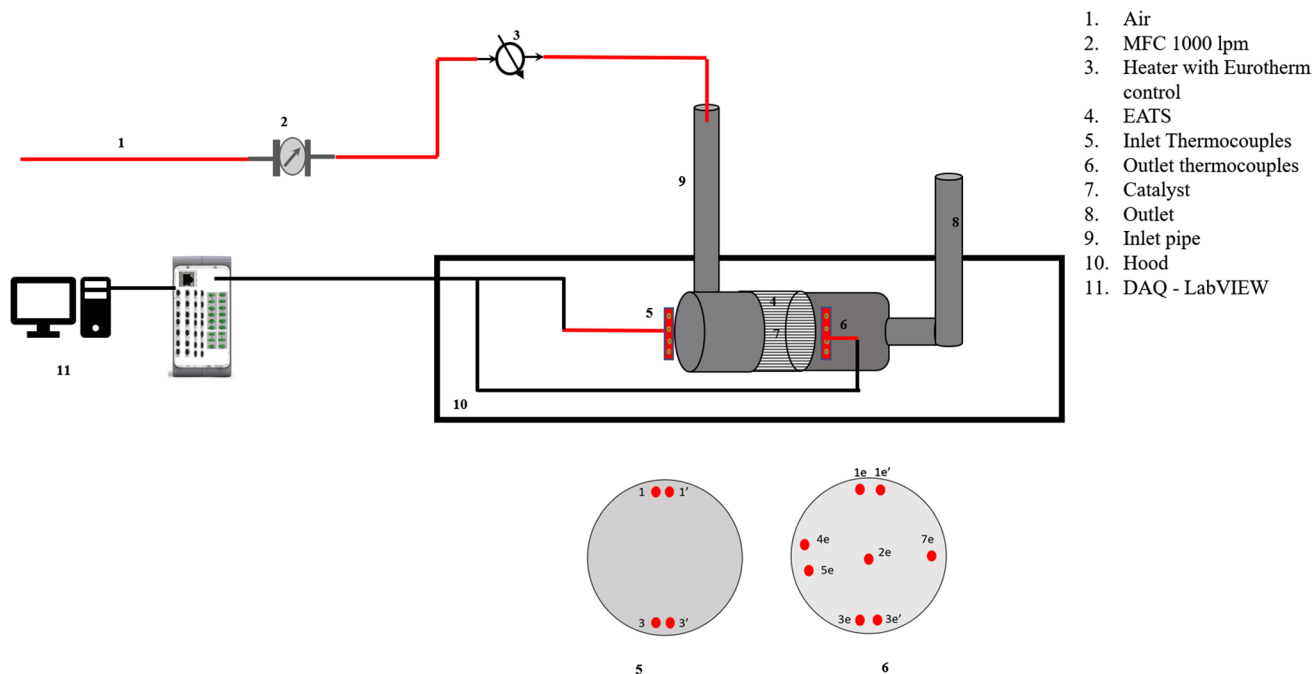
| Variable | Description |
|---|---|
| $A_i$ | Face area |
| $C_p$ | Specific heat capacity |
| $C_i$ | Coefficient of viscous resistance for porous media |
| $E_f$ | Total fluid energy |
| $E_s$ | Total solid medium energy |
| $I$ | Identity matrix |
| $I_{turb}$ | Turbulent intensity |
| $k_{eff}$ | Effective thermal conductivity of the fluid and solid phase |
| $k_s$ | Thermal conductivity of the solid phase in porous media |
| $n$ | Number of cells |
| $\overline{p}$ | Mean pressure in vector notation |
| $q_i$ | Heat flux vector |
| $Re$ | Reynolds number |
| $S$ | Strain tensor |
| $S_i$ | Source term for porous media |
| $S_f^h$ | Enthalpy source term for fluid |
| $t$ | Time |
| $\overline{T}$ | Mean temperature |
| $\overline{U_i}$ | Mean velocity in tensor notation |
| $\overline{u_i'}$ | Fluctuating velocity in tensor notation |

| Variable | Description |
|---|---|
| $\overline{v}$ | Phase velocity |
| $x_i$ | Position vector in tensor notation |
| $\beta_1$ | Closure constant |
| $\beta^*$ | Closure constant |
| $\gamma_1$ | Ratio of $\beta^*$ and $\beta_1$ |
| $\gamma_a$ | Flow uniformity index |
| $\epsilon$ | Porosity of the porous media |
| $\kappa$ | Turbulent kinetic energy |
| $\lambda$ | Thermal conductivity of fluid |
| $\mu$ | Molecular viscosity |
| $\mu_t$ | Turbulent viscosity |
| $\nabla$ | Gradient operator |
| $\rho$ | Density of fluid |
| $rho_f$ | Fluid density |
| $rho_s$ | Solid medium density |
| $\sigma_k$ | Turbulent Prandtl number for turbulent kinetic energy |
| $\sigma_\omega$ | Turbulent Prandtl number for turbulent dissipation rate |
| $\Phi$ | Dissipation function |
| $\phi_i$ | Flow variable |
| $\overline{\phi_a}$ | Area weighted flow variable |
| $\omega$ | Turbulent dissipation rate |

# Appendix B. Tuning of Heat Transfer Coefficients

Experiments were performed to obtain realistic estimates of the heat transfer coefficients and can be used in the simulations. As the heat losses are very influential on both the flow and temperature uniformity evolution, this is deemed as an important step in correctly reflecting the true complexity of the chosen geometry (the so-called academic EATS).



1. Air
2. MFC 1000 lpm
3. Heater with Eurotherm control
4. EATS
5. Inlet Thermocouples
6. Outlet thermocouples
7. Catalyst
8. Outlet
9. Inlet pipe
10. Hood
11. DAQ - LabVIEW

**Fig. 15** Schematic of the experimental rig. The shaded region is the catalyst. The thermocouple inserts are shown by red dots at the inlet and outlet planes. Four thermocouples are placed on the inlet side and 8 thermocouples are placed on the outlet

**Table 5** Position of the thermocouples placed

| Point | x-coordinate | y-coordinate | z-coordinate | Location |
|---|---|---|---|---|
| Point 1e | −0.007 | 0.043 | 0.1705 | Outlet |
| Point 1e' | 0.007 | 0.043 | 0.1705 | Outlet |
| Point 2e | 0 | 0 | 0.1705 | Outlet |
| Point 3e | −0.007 | −0.043 | 0.1705 | Outlet |
| Point 3e' | 0.007 | −0.043 | 0.1705 | Outlet |
| Point 4e | −0.034 | 0.008 | 0.1705 | Outlet |
| Point 5e | −0.039 | 0.008 | 0.1705 | Outlet |
| Point 6e | 0.039 | 0.008 | 0.1705 | Outlet |
| Point 1 | 0.007 | −0.043 | 0.025 | Inlet |
| Point 1' | −0.007 | −0.043 | 0.025 | Inlet |
| Point 3 | 0.007 | 0.043 | 0.025 | Inlet |
| Point 3' | −0.007 | 0.043 | 0.025 | Inlet |

Steady-state simulations were performed to tune the heat loss to the ambient through the heat transfer coefficients. Experimental values of temperatures were logged using thermocouples, by passing heated air at the tested flowrates (500 lpm and 948 lpm). The temperatures measured were compared with that predicted by the simulations. This provided a means to tune heat transfer coefficients for use in the transient simulations. The tuning is accomplished using the method of least squares. These results (in terms of the sum of squares for the error, SSE) are shown in Figs. 16 and 17. The numerical values of the heat transfer coefficients ultimately used were $h = 10$ W/m$^2$,K for the horizontal pipe in both cases, and $h = 50$ and $100$ W/m$^2$,K for the vertical pipe at 500 lpm and 948 lpm, respectively.
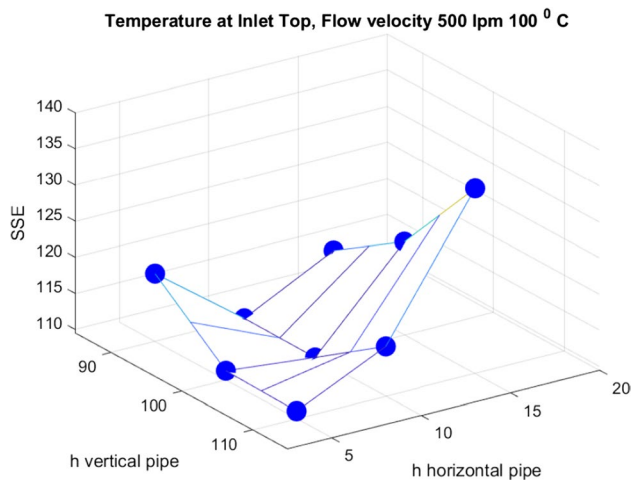


**Fig. 17** Minimum of SSE for 948 lpm
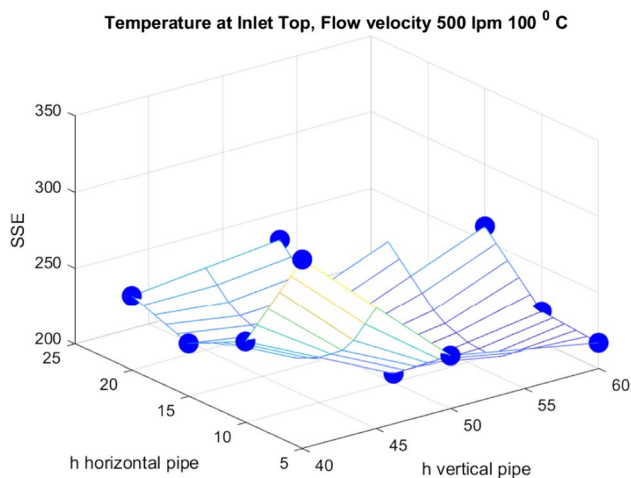


**Fig. 16** Minimum of SSE for 500 lpm

# Appendix B. Notes on the Definition of UI, the Choice of Reference Base Values, and their Implication

The uniformity index (UI) is defined in Eq. 1. This definition involves the relative difference between a flow variable and its mean value, taken over $n$ points in the flow surface. Depending on the definition of flow variable of interest, an alternative variable can be defined such that the value of the UI well represents the spread or nature of the distribution. The role of the definition of the variable in question can be explained by an example considering temperature. The histogram of temperature in Fig. 4 shows a considerable spread. One would thus expect a UI value that is not equal to 1 for temperature. However, when using the temperature in Kelvin units, the value of UI is above 0.99. This value of UI confounds the notion of uniformity of temperature field, as the variations are small in relation to the absolute temperature. Therefore, it is imperative to use an alternative definition for the variable to represent temperature in the current case. By simply deducting a reference base value (such as the ambient temperature, as the temperature within the system can never be below this value), the absolute values acquired for the UI in question are remarkably lower — even though the temperature information itself has not been manipulated. Table 6 lists a comparison between some different definitions and the resulting UI for the current work.

**Table 6** Uniformity index at plane P4 (domain outlet) for different definitions of the velocity and temperature UIs, respectively. Here, $|T|$ implies using the absolute temperature in Kelvin to calculate the temperature UI according to Eq. 1, whereas $|T - 273.15|$ indicates that one first deducts a reference background value of 273.15 K from the entire temperature field before calculating the corresponding UI, and so on

| Definition | UI at P4 |
|---|---|
| $\|V\|$ (m/s) | 0.9098 |
| $\|V - 1\|$ (m/s) | 0.8262 |
| $\|V - 4\|$ (m/s) | 0.9022 |
| $\|V - 10\|$ (m/s) | 0.9763 |
| $\|T\|$ (K) | 0.9932 |
| $\|T - 273.15\|$ (K) | 0.9680 |
| $\|T - 290.15\|$ (K) | 0.9585 |
| $\|T - 330.15\|$ (K) | 0.8325 |

## Declarations

**Conflict of Interest** The authors declare that they have no competing interests.

## References

1. Reşitoğlu, İA., Altinişik, K., Keskin, A.: The pollutant emissions from diesel-engine vehicles and exhaust aftertreatment systems. Clean Technol. Environ. Policy **17**(1), 15–27 (2015)
2. Manisalidis, I., Stavropoulou, E., Stavropoulos, A., Bezirtzoglou, E.: Environmental and health impacts of air pollution: a review. Front. Public Health **8**, 14 (2020)
3. Heck, R.M., Farrauto, R.J., Gulati, S.T.: Catalytic air pollution control: commercial technology. Wiley, Hoboken (2016)
4. Emissions in the automotive sector. Available from: https://ec.europa.eu/growth/sectors/automotive-industry/environmental-protection/emissions-automotive-sector_en. https://www.europarl.europa.eu/RegData/etudes/BRIE/2022/698920/EPRS_BRI(2022)698920_EN.pdf. Accessed 29 Apr 2022
5. Koltsakis, G.C., Stamatelos, A.M.: Catalytic automotive exhaust aftertreatment. Prog. Energy Combust. Sci. **23**(1), 1–39 (1997)
6. Benjamin, S.F., Liu, Z., Roberts, C.A.: Automotive catalyst design for uniform conversion efficiency. Appl. Math. Model. **28**(6), 559–572 (2004)
7. Heck, R., Hu, Z., Smaling, R., Amundsen, A., Bourke, M.: Close coupled catalyst system design and ULEV performance after 1050 C aging. SAE transactions 1217–1222 (1995)
8. Jeong, S.J.: A full transient three-dimensional study on the effect of pulsating exhaust flow under real running condition on the thermal and chemical behavior of closed-coupled catalyst. Chem. Eng. Sci. **117**, 18–30 (2014)
9. EU: Cars and Light Trucks: RDE Testing. Available from: https://dieselnet.com/standards/eu/ld_rde.php. Accessed 29 Apr 2022
10. Young, L.C., Finlayson, B.A.: Mathematical models of the monolith catalytic converter: part I. Development of model and application of orthogonal collocation. AIChE Journal **22**(2), 331–343 (1976)
11. Young, L.C., Finlayson, B.A.: Mathematical models of the monolith catalytic converter: Part II. Application to automobile exhaust. AIChE J **22**(2), 343–353 (1976)
12. Oh, S.H., Cavendish, J.C.: Transients of monolithic catalytic converters. Response to step changes in feedstream temperature as related to controlling automobile emissions. Industrial & Engineering Chemistry Product Research and Development **21**(1), 29–37 (1982)
13. Kirchner, T., Eigenberger, G.: On the dynamic behavior of automotive catalysts. Catal. Today **38**(1), 3–12 (1997)
14. Santos, H., Costa, M.: Modelling transport phenomena and chemical reactions in automotive three-way catalytic converters. Chem. Eng. J. **148**(1), 173–183 (2009)
15. Siemund, S., Leclerc, J., Schweich, D., Prigent, M., Castagna, F.: Three-way monolithic converter: simulations versus experiments. Chem. Eng. Sci. **51**(15), 3709–3720 (1996)
16. Hoebink, J., Van Gemert, R., Van Den Tillaart, J., Marin, G.: Competing reactions in three-way catalytic converters: modelling of the NOx conversion maximum in the light-off curves under net oxidising conditions. Chem. Eng. Sci. **55**(9), 1573–1581 (2000)
17. Holder, R., Bollig, M., Anderson, D., Hochmuth, J.: A discussion on transport phenomena and three-way kinetics of monolithic converters. Chem. Eng. Sci. **61**(24), 8010–8027 (2006)
18. Lundberg, B., Sjoblom, J., Johansson, Å, Westerberg, B., Creaser, D.: Parameter estimation of a DOC from engine rig experiments with a discretized catalyst washcoat model. SAE Int. J. Engines **7**(2), 1093–1112 (2014)
19. Walander, M., Sjöblom, J., Creaser, D., Agri, B., Löfgren, N., Tamm, S., et al.: Modelling of mass transfer resistances in non-uniformly washcoated monolith reactors. Emiss. Control Sci. Technol. **7**(2), 153–162 (2021)
20. Gupta, N., Balakotaiah, V.: Heat and mass transfer coefficients in catalytic monoliths. Chem. Eng. Sci. **56**(16), 4771–4786 (2001)
21. Weltens, H., Bressler, H., Terres, F., Neumaier, H., Rammoser, D.: Optimisation of catalytic converter gas flow distribution by CFD prediction. SAE Technical Paper 930780 (1993)
22. Holmgren, A., Grönstedt, T., Andersson, B.: Improved flow distribution in automotive monolithic converters. React. Kinet. Catal. Lett. **60**(2), 363–371 (1997)
23. Agrawal, G., Kaisare, N.S., Pushpavanam, S., Ramanathan, K.: Modeling the effect of flow mal-distribution on the performance of a catalytic converter. Chem. Eng. Sci. **71**, 310–320 (2012)
24. Dammalapati, S., Aghalayam, P., Kaisare, N.: Modeling the effects of the inlet manifold design on the performance of a diesel oxidation catalytic converter. Ind. Eng. Chem. Res. **60**(10), 3860–3870 (2021)
25. Mu, M., Sjöblom, J., Ström, H., Li, X.: Analysis of the flow field from connection cones to monolith reactors. Energies **12**(3), 455 (2019)
26. Chakravarthy, V., Conklin, J., Daw, C., D'Azevedo, E.: Multi-dimensional simulations of cold-start transients in a catalytic converter under steady inflow conditions. Appl. Catal. A **241**(1–2), 289–306 (2003)
27. Martin, A., Will, N., Bordet, A., Cornet, P., Gondoin, C., Mouton, X.: Effect of flow distribution on emissions performance of catalytic converters. SAE transactions 384–390 (1998)
28. ANSYS, Inc.: ANSYS FLUENT Theory Guide. ANSYS, Canonsburg, PA (2021)
29. Munnannur, A., Cremeens, C.M., Liu, Z.G.: Development of flow uniformity indices for performance evaluation of aftertreatment systems. SAE Int. J. Engines **4**(1), 1545–1555 (2011)
30. Germidis, A., Castagna, F., Banaigs, J.: Thermal measurements inside a three-way catalytic converter on engine bench. SAE Technical Paper 930624 (1993)
31. Wilcox, D.C., et al.: Turbulence modeling for CFD, vol. 2. DCW industries La Canada, CA (1998)
32. Menter, F.R.: Two-equation eddy-viscosity turbulence models for engineering applications. AIAA J. **32**(8), 1598–1605 (1994)
33. Chen, M., Aleixo, J., Williams, S., Leprince, T., Yong, Y.: CFD modelling of 3-way catalytic converters with detailed catalytic surface reaction mechanism. SAE Technical Paper 2004-01-0148 (2004)

**Publisher's Note** Springer Nature remains neutral with regard to jurisdictional claims in published maps and institutional affiliations.